Characterisation and constitutive model of tensile properties of selective laser melted Ti-6Al-4V struts for microlattice structures

Zhiyong Wang [a], Peifeng Li [b,*]

[a] School of Mechanical and Aerospace Engineering, Nanyang Technological University, Singapore

[b] School of Engineering, University of Glasgow, Glasgow, UK

[*] Corresponding author's email: peifeng.li@glasgow.ac.uk (P. Li); Tel: +44 141 330 2703.

Abstract

Predicting the mechanical performance of selective laser melted (SLM) microlattice structures requires the constitutive data of the parent solid material in the struts. This work first characterised the cross-sectional features of individual SLM Ti-6Al-4V struts. The direct examination revealed the non-linear relation between the equivalent diameter and the Feret diameter of a strut, which was quantified by an empirical equation. The equation considering surface roughness effects allowed the non-destructive determination of the equivalent diameter using the directly measured Feret diameter prior to tension testing. Uniaxial tension experiments were then performed to accurately measure the constitutive behaviour of SLM Ti-6Al-4V struts, with the strain history tracked and recorded using high resolution imaging. It was found that the strut diameter ranging 300–1200 μm has a negligible effect on the stress–strain response. The strain hardening and fracture behaviour of the SLM Ti-6Al-4V can be quantitatively described using the Johnson–Cook models with damage. The constitutive models were finally validated by the 3D finite element model and experiments of uniaxial compression on an SLM microlattice structure. The methodology presented here can accurately characterise and formulate the constitutive behaviour of SLM metallic struts for microlattices.

Keywords: Constitutive equation; Strain measurements; Titanium alloys; Selective laser melting (SLM); Finite element model.

1 Introduction

Metallic microlattice structures with regular unit cell topologies and dimensions have received considerable attentions for the past decades in many potential applications ranging from automotive, aerospace to biomedical parts due to their light weight and good specific properties [1-6]. The recent development in additive manufacturing technologies such as selective laser melting (SLM) enables the fabrication of metallic microlattices with more complicated architectures and better tailorability of properties [6-11]. The bulk deformation behaviour of microlattices is not only influenced by the periodic unit cell features but also by the local material properties of individual solid struts in the microlattice. The finite element (FE) simulation revealed that localised tensile and compressive stress states significantly determine the crack propagation modes in the struts of SLM stainless steel 316L microlattices [8]. Thus, to predict the mechanical performance of microlattices it is necessary to accurately characterise and formulate the constitutive behaviour of the parent solid material.

A large portion of studies has been reported on the mechanical behaviour of bulk SLM metals, for example, stainless steel [1, 6-8], titanium alloys [12, 13] and aluminium alloys [4, 14]. The processing parameters (e.g., laser power, scanning speed, hatch spacing and layer thickness) and their interactions can significantly affect the microstructure formation during the solidification, and finally determine the resultant properties of the SLM metal [4, 15-19]. A mixture of α phase, β phase and acicular martensitic α' phase has been observed in the SLM Ti-6Al-4V microstructure

[15, 20]. The presence of acicular martensites in the SLM Ti-6Al-4V leads to the significant improvement in tensile strength from 900 to 1450 MPa but the considerably reduced ductility [20-22]. Subsequent heat treatment at intermediate to high temperatures can further control and optimise the mechanical properties of the SLM Ti-6Al-4V [23].

To achieve lighter weight, the struts in metallic microlattices often have the diameter down to a few hundred microns [4, 6, 8, 11, 17]. In the SLM process, the thermal history in thin struts may be rather different from that in bulk metals, thus leading to the dissimilarity in microstructure and mechanical properties between them. Therefore, the constitutive description obtained directly from individual struts instead of bulk SLM metals is more suitable for the simulation of mechanical response of microlattices [1, 8, 17, 24]. However, only few studies in the literature focused on the characterisation and constitutive model of the tensile properties of individual struts [1, 8, 17]. The rough surface of struts affects the accuracy in the non-destructive measurement of geometrical characteristics, especially the effective cross-sectional area (or equivalent diameter) that is relevant to the determination of stresses. Nevertheless, most of the existing work neglected the impact of surface roughness on the measurement in a strut's geometry.

The aim of the study reported here is to accurately characterise the constitutive behaviour of SLM Ti-6Al-4V struts and then quantitatively formulate this behaviour using empirical models. The transverse cross sections of SLM struts with nominal diameter D = 300–1200 μm were examined in scanning electron microscope (SEM)

and analysed to correlate the equivalent diameter D_e to the Feret diameter D_F. This relation provided a non-destructive way to estimate the D_e from the directly measured D_F. Uniaxial tension tests were carried out to measure the stress–strain response and the fracture behaviour of the struts. The strain history in the strut was precisely tracked using the recorded high resolution images. The Johnson–Cook (J–C) models with damage were used to formulate the constitutive behaviour. The developed models were finally applied to an FE model of uniaxial compression of SLM microlattices and validated by the experiments.

2 Experimental procedure

2.1 Materials and specimen preparation

The Ti-6Al-4V struts for tension tests (Fig. 1) were manufactured in the selective laser melting system SLM-250HL (SLM Solutions GmbH, Germany). The argon atomised Ti-6Al-4V powders (TLS Technik GmbH & Co, Germany) used in the SLM process feature extra low interstitials (ELI), with the chemical composition listed in Table 1. The diameter of the powders ranges within 20–63 μm [15]. The SLM machine uses an ytterbium laser source with the focus diameter 70 μm and operating in the Gaussian distribution mode. The argon atmosphere was introduced to ensure the oxygen level less than 0.02% within the working chamber of the SLM machine. The substrate was pre-heated and maintained at 200°C during the SLM. The laser power 120 W, the scanning speed 400 mm s^{-1}, the hatch spacing 80 μm and the layer thickness 50 μm were applied in the SLM to achieve the low porosity, large

martensitic lath size and subsequent high strength [15]. Details on the SLM technique employed in the present research can be found in the literature [15].

The SLM Ti-6Al-4V strut specimens comprised (1) the cylindrical gauge with length 10 mm and different nominal gauge diameters D = 300, 400, 600, 900 and 1200 μm, and (2) the flat ends for clamping (Fig. 1). Fig. 2 schematically illustrates the key dimensions of the "dog-bone" shaped strut specimen for tension tests. The width of the flat ends increased with the gauge diameter in order to enhance the gripping effect.

2.2 Characterisation of microstructure and cross-sectional features of struts

The gauge portion of several strut specimens was transversely cut at a number of locations (refer to Fig. 2). These transverse cross sections were ground, polished and then examined in the JEOL JSM-7600F SEM (JEOL Ltd., Japan) to characterise both the microstructure and the geometrical features. As shown in Fig. 3, the acicular martensitic microstructure typically occurred in the SLM Ti-6Al-4V as a result of the enormously rapid cooling rate during the solidification in the SLM process. The average martensitic lath size was approximately 40 μm, consistent with the previous observations on the bulk SLM Ti-6Al-4V manufactured using the same SLM parameters and powders [15].

Fig. 4 illustrates the cross sections of the individual SLM struts with various nominal diameters. The surface of the struts is rough mainly due to the unmelted

powders. The roughness can affect the measurement accuracy of the diameter of struts. The diameter directly measured (e.g., using a calliper), called the Feret or calliper diameter (D_F), is usually the maximum distance of two peaks on the rough surface. The use of Feret diameter results in the overestimation of the cross-sectional area especially for the struts with smaller nominal diameters, thus underestimating the stress-related properties of the material such as Young's modulus and yield strength. The SEM images of these cross sections (Fig. 4) were quantitatively analysed in the ImageJ software to calculate the cross-sectional properties including Feret and equivalent diameters and then to formulate their relation.

2.3 Uniaxial tension tests

Uniaxial tension tests were performed on the SLM Ti-6Al-4V strut specimens to measure the stress–strain behaviour in an INSTRON (INSTRON, MA, USA) electromechanical universal testing machine under the displacement control mode (speed 0.01 mm s^{-1}, thus strain rate 0.001 s^{-1}). An in-house gripping fixture with the flat rough textured jaw faces was utilised to firmly clamp the strut and reduce the slippage between the specimen and the jaw faces [8]. The universal joint in the fixture minimised the misalignment effect during the tension experiments. The applied force was directly measured by the calibrated load cell. The deformation process of the strut specimens was recorded in a JAI (JAI Ltd., Japan) BM-500 GE high resolution camera at ~12.5 μm per pixel. The white stripes marked on the specimen surface to improve the image contrast were tracked to accurately calculate the deformation

history of the specimen. The stress and the strain were finally quantified from the measured force and deformation, respectively.

After the tension tests, the fracture surface of individual struts was characterised in the SEM to reveal the failure mechanism of SLM Ti-6Al-4V alloys under tension. The fracture area was also quantitatively estimated to determine the strength and strain at fracture. Uniaxial tension experiments were repeated on at least four strut specimens of each nominal diameter.

3 Results and discussion

3.1 Relation of the equivalent and Feret diameters of an SLM strut

Due to the nature of the SLM process, the surface of individual Ti-6Al-4V struts is rough, and the transverse cross section is not a perfect circle especially in the struts with the smaller nominal diameter (Fig. 4). The Feret diameter D_F that can be measured directly is often greater than the equivalent diameter D_e defined by the effective transverse cross-sectional area A_{eff}.

$$D_e = \sqrt{\frac{4\,A_{eff}}{\pi}} \tag{1}$$

To quantify the constitutive behaviour of SLM Ti-6Al-4V, it is necessary to precisely measure and use the transverse cross-sectional area of the strut and thus the equivalent diameter. In tension experiments, the equivalent diameter of struts must be determined non-destructively. The 3D rough feature of strut surfaces can be reconstructed using x-ray microtomography for the measurement of equivalent

diameters; however, this method is time-consuming and cost-ineffective. In this section, a quantitative relation between the equivalent diameter and the Feret diameter was developed for the struts with nominal diameters ranging from 300–1200 μm using SEM images of sectioned struts (a destructive method). Therefore, in tension tests the equivalent diameter can be estimated from the measured Feret diameter in a non-destructive way, using this relation.

The SEM images of the cross sections (Fig. 4) were discretised into pixels. The cross-sectional area $A(i)$ at the ith cutting location in the strut can then be estimated based on the number of pixels $p(i)$:

$$A(i) = p(i) \times (r(i))^2 \tag{2}$$

where $r(i)$ is the spatial resolution of the SEM image of the cross section. This estimation was valid as the number of pixels was very large (usually >400 000 in the SEM images). The effective transverse cross-sectional area A_{eff} of the strut was thus the average of the transverse areas in all the cutting locations:

$$A_{\text{eff}} = \frac{1}{n}\sum_{i=1}^{n} A(i) = \frac{1}{n}\sum_{i=1}^{n}\left(p(i) \times (r(i))^2 \right) \tag{3}$$

where n is the number of cutting locations ($n \geq 3$). Finally the equivalent diameter D_{e} was calculated by the effective area A_{eff} using Eq. (1).

Fig. 5(a) quantitatively demonstrates the equivalent diameter and the Feret diameter of the individual struts. Note that the Feret diameter D_{F} was directly measured as the maximum distance of two parallel tangent lines among the cutting sections in the SEM images (refer to Fig. 4). For a given Ti-6Al-4V powder

distribution and the specific SLM processing parameters, the surface roughness of struts can be assumed constant regardless of the nominal diameter. As shown in Fig. 5(a), the equivalent diameter is less than the Feret diameter (i.e., the data below the 1:1 line). However, for the struts with larger nominal diameters, their equivalent diameter approximates to the Feret diameter, i.e., the data in Fig. 5(a) approaches the 1:1 line as D_F increases. Therefore, a non-linear relation is expected between D_e and D_F.

In order to find a suitable formula for the non-linear relation between D_e and D_F, a shape factor S of the transverse cross section was introduced as follows.

$$S = \frac{A_{\text{eff}}}{\pi D_F^2 / 4} = \frac{\pi D_e^2 / 4}{\pi D_F^2 / 4} = \frac{D_e^2}{D_F^2} \tag{4}$$

The shape factor is equal to 1.0 in a perfect circle. The shape factor was calculated for the individual struts as shown in Fig. 5(b); and it varied with the measured Feret diameter non-linearly in a more noticeable fashion. A regression analysis was thus performed to correlate the shape factor and the Feret diameter using the exponent function,

$$S = 1 - \exp(-kD_F) \tag{5}$$

where k is the fitted parameter. A correlation coefficient R^2 = 0.90 was achieved for the regression (k = 0.0025 μm^{-1}). Note that the measured data of the struts with the nominal diameter D = 600 μm was excluded from the regression analysis; instead it was used to validate the regression (Fig. 5(b)). Substituting the shape factor S in

Eq. (4) into Eq. (5) resulted in the direct relation between the equivalent diameter of a strut and its Feret diameter.

$$D_e = D_F\sqrt{1-\exp\left(-kD_F\right)} \tag{6}$$

The regression for D_e over D_F achieved a correlation coefficient R^2 = 0.98 with the fitted parameter k = 0.0023 μm^{-1} (Eq. (6)), which is very close to the fitted parameter (k = 0.0025 μm^{-1}) for S and D_F relation (Eq. (5)). Again, the data for D = 600 μm was only used for validation in this regression analysis (Fig. 5(a)).

3.2 Tensile deformation behaviour of individual struts

Fig. 6(a) shows the typical stress–strain curve of an SLM Ti-6Al-4V strut with the nominal diameter D = 600 μm. Prior to the tension test, the equivalent diameter of the strut was determined in terms of the diameter (Feret) measured by the calliper using Eq. (6). The stress was then calculated using the equivalent diameter and the measured applied force. The optical images of the deformation sequence recorded in the JAI camera (Fig. 6(b)) were analysed to track the black/white edges and then calculate the strain history of the specimen. The strains corrected by the images were significantly less than those directly measured in the INSTRON machine by a factor of ~2.7 in the elastic region (~1.9 in the plastic region). This implies that the slippage effect is still considerable between the specimen and the jaw faces regardless of the rough texture of the faces [8, 25]. However, the use of high resolution images (the non-contact technique) can accurately record strains in the specimen despite the slippage effect.

The representative stress–strain responses of struts with different nominal diameters D = 300, 400, 600, 900 and 1200 μm are illustrated in Fig. 7(a–e). A good repeatability of <2% was achieved for the tension tests on the struts of the same diameters. The averages of the stress–strain curves were quantified for these five types of struts, as shown in Fig. 7(a–e) and re-plotted in Fig. 7(f). There is no obvious trend on the effect of nominal diameter on the stress–strain behaviour of thin struts with D ranging from 300 to 1200 μm (compare the curves in Fig. 7(f)). The variation due to the strut diameter is less than 4%. The ultimate average (the dashed line in Fig. 7(f)) was calculated from these individual averages (Fig. 7(a–e)) of the struts of different diameters, and was then used for the constitutive formulation of SLM Ti-6Al-4V material.

The Young's modulus E = 107±3 GPa is very close to the modulus (110–120 GPa) of bulk Ti-6Al-4V alloys manufactured by conventional techniques. This indicates that the SLM process parameters may be reasonable. The slightly lower value of the modulus in SLM Ti-6Al-4V is probably a result of the presence of pores in the struts [8, 26, 27]. The yield strength is σ_y = 997±42 MPa as defined at the intersection of the elastic and plastic regions. This high strength is due to the acicular martensitic microstructure (Fig. 3).

3.3 Fracture behaviour of SLM Ti-6Al-4V

During the tension tests, most of the SLM Ti-6Al-4V strut specimens failed in the middle of the gauge portion (Fig. 6(b)). This suggests that the misalignment effect

was minimised because of the use of the universal joint in the in-house gripping fixture. Post-test examination in the SEM reveals the fracture features of the specimens with minor necking (Fig. 8). In all the struts under tension, the fracture initiated in the defects such as the pores (Fig. 8(a–c)). Note that unmelted powders can often be present in the pores (Fig. 8(c)). Tilted planes, for example 20° to 45° to the transverse cross section, can be observed in part of the fracture surface. A detailed examination reveals the substantial dimples (plastic deformation) occurring in the fracture surfaces (Fig. 8(d)). Therefore, the fracture of SLM Ti-6Al-4V is ductile. However, compared to conventional Ti-6Al-4V alloys, the relatively lower ductility in SLM Ti-6Al-4V is due to the acicular martensitic microstructure.

The fracture surface observed along the longitudinal direction in the SEM was analysed to quantify the effective fracture area in the transverse plane (A_f). Note that the fracture area excluded the pore that served as the fracture crack initiator. The true stress at fracture ($\sigma_f = F_f/A_f$) was equal to the measured fracture force (F_f) divided by the effective fracture area. With the assumption of the constant specimen volume during plastic deformation, the equivalent plastic strain at fracture ($\varepsilon_f = \ln(A_{eff}/A_f)$) was estimated from the original effective transverse area (A_{eff}) and the fracture area (A_f). The fracture strength σ_f and the corresponding fracture strain ε_f are shown in Fig. 9. The scatter in fracture strain ranging from 0.07 to 0.2 might be due to the variation of the transverse cross-sectional shape (S) and the porosity in strut specimens. Based on the constant volume assumption, the true stress (σ) and the true

plastic strain (ε_{pl}) during the tensile deformation process of struts (Fig. 9) were also calculated from the ultimate average stress–strain data (Fig. 7(f)).

3.4 Constitutive models of SLM Ti-6Al-4V

As shown in Fig. 9, the true plastic strain that can be measured directly prior to fracture was less than 0.02. The strains ranging between 0.02 and the fracture strain were not obtained during the minor necking process. To fill this gap and develop the constitutive equation of SLM Ti-6Al-4V, the empirical Johnson–Cook hardening model was used to formulate the flow stress (σ) as a function of true plastic strain (ε_{pl}) [28],

$$\sigma = \left[A + B\,\varepsilon_{pl}{}^{n} \right] \left[1 + C \ln\left(\dot{\varepsilon}_{pl}^{*}\right) \right] \left[1 - \left(T^{*}\right)^{m} \right] \tag{7}$$

where A, B, C, m, and n are the material constants, $\dot{\varepsilon}_{pl}^{*}$ is the dimensionless plastic strain rate, and T^{*} is the dimensionless temperature. Furthermore, the J–C failure model can define the variation of the equivalent plastic strain at fracture (ε_f) with the stress triaxiality factor σ^{*},

$$\varepsilon_f = \left[D_1 + D_2 \exp\left(D_3 \sigma^{*}\right) \right] \left[1 + D_4 \ln\left(\dot{\varepsilon}_{pl}^{*}\right) \right] \left[1 - D_5 T^{*} \right] \tag{8}$$

where D_1, D_2, D_3, D_4, and D_5 are the damage constants. The second and third terms in both Eqs. (7) and (8) represent the strain rate and temperature dependencies. The uniaxial tension tests in the present study were performed at the constant quasi-static strain rate ($0.001\ s^{-1}$) at room temperature. Thus, the J–C hardening and failure models can be simplified as follows without considering the strain rate and temperature effects.

$$\sigma = A + B\,\varepsilon_{\mathrm{pl}}{}^{n} \tag{9}$$

$$\varepsilon_{\mathrm{f}} = D_1 + D_2 \exp\left(D_3 \sigma^*\right) \tag{10}$$

The stress triaxiality factor σ^* can be typically estimated according to the failure process using this formula [29]:

$$\sigma^* = \frac{1}{3} + \ln\left(1 + \frac{a_0}{2R}\right) \tag{11}$$

where a_0 is the original specimen radius at the notch centre and R is the notch radius. For the strut specimens manufactured by the SLM, it can be assumed that $a_0 = D_e/2$ and $R = (D_F - D_e)/4$. Hence, the stress triaxiality factor σ^* can be approximated and rewritten as a function of D_e/D_F.

$$\sigma^* = \frac{1}{3} + \ln\left(\frac{1}{1 - D_e/D_F}\right) \tag{12}$$

Fig. 10 shows the calculated stress triaxiality factors of the tested strut specimens.

The strain hardening and fracture behaviour of the SLM Ti-6Al-4V can be quantitatively characterised by the J–C constitutive models (Eqs. (9) and (10)). The measured stress–strain data prior to fracture was analysed to fit the constitutive hardening model Eq. (9) (refer to Fig. 9). The failure model Eq. (10) was used to regress the data at fracture as shown in Fig. 10. Table 2 lists the fitted parameters of the J–C models. The stress–strain curve was extrapolated to the large strains up to fracture. The fitted curve passes the measured data at fracture, suggesting a good fit of the J–C hardening model. As fracture is sensitive to defects, the large scatter in fracture strains leads to the fit of the fracture model with a smaller correlation

coefficient (Fig. 10). This indicates that careful characterisation of material failure should be made to obtain the material constants for fracture.

3.5 Application to SLM microlattice structures

The developed J–C constitutive models with damage for the SLM Ti-6Al-4V were input to a 3D finite element model of the uniaxial compression on a microlattice structure. The FE model was established in the ABAQUS/Explicit software ((Dassault Systèmes Simulia Corp., RI, USA). The microlattice structure consisted of 6×6×6 body centred cubic (BCC) unit cells. The edge length of the unit cell was 2.53 mm and the strut diameter 300 μm (Fig. 11(a)). Note that Fig. 11(a) only demonstrates the front view of the 3D microlattice. The full geometry of the microlattice was modelled and meshed with the quadratic tetrahedral elements. A general contact property of a friction coefficient 0.06 was assumed for all the external surfaces. The FE elements were deleted when the damage occurred in the corresponding part of the microlattice. Details on the FE model were similar to the previous model about an SLM stainless steel 316L microlattice [1, 8].

To validate the FE model and the developed J–C formulation, the Ti-6Al-4V microlattice structures (6×6×6 BCC unit cells, cell edge length 2.53 mm and strut nominal diameter 300 μm) were fabricated in the SLM machine using the same processing parameters as those for the individual struts (Fig. 11(a)). Uniaxial compression on the microlattices was performed at the quasi-static rate 0.001 s^{-1} in the INSTRON machine, with the deformation history recorded in the JAI camera. Note

that the bottom of the microlattice was a plate when manufactured whilst the top was open. The experimental observations on the boundary and loading conditions were applied to the FE model.

Fig. 12 illustrates the stress–strain curves of the microlattices under uniaxial compression. Note that the plastic strain was used. Both the FE prediction and experimental measurements reveal the consistent profile of the curves, which consist of the oscillating plateau and final densification stages similar to the deformation behaviour of open-cell foams [30]. A sudden drop in stress observed after the initial peak stress corresponds to the collapse of struts occurring along the 45° diagonal plane (Fig. 11(b)), probably due to the relatively low ductility in the SLM Ti-6Al-4V. A good agreement was also found between the local damage experimentally observed in the struts and the deletion of FE elements in the model. These similarities validate the developed FE model of microlattices and the fitted parameters of the J–C constitutive models for the SLM Ti-6Al-4V. Some dissimilarities exist, for instance, the relatively faster drop of stress at the peak in the FE model may be attributed to the assumption of idealised struts that overlook the surface roughness effect.

4 Conclusions

Tensile constitutive behaviour was accurately characterised and quantitatively formulated for selective laser melted Ti-6Al-4V struts with nominal diameters D = 300–1200 μm. The conclusions were drawn as follows.

- Due to the surface roughness, the equivalent diameter D_e of a strut is less than the Feret diameter D_F, but D_e becomes approximate to D_F as the diameter increases. This non-linear relation between D_e and D_F can be quantified using an empirical equation. This equation allows the non-destructive estimation of original D_e based on the measured D_F prior to tension tests.

- There is no obvious trend on the influence of strut diameter on the stress–strain behaviour of individual struts. The fracture of SLM Ti-6Al-4V is ductile. However, as a result of the formed acicular martensitic microstructure, the ductility is less than that of conventional Ti-6Al-4V alloys whilst the yield strength is higher.

- The J–C hardening model can quantify the stress–strain response in plastic deformation. The final fracture behaviour can be formulated by the variation of the fracture strain with the stress triaxiality factor using the J–C failure model. The uniaxial compression experiments of SLM microlattices and the 3D finite element model of the experiment validated the developed J–C constitutive models with damage for SLM Ti-6Al-4V.

Acknowledgements

The authors gratefully acknowledge the financial support of Academic Research Fund (AcRF) Tier 1 by Ministry of Education, Singapore (Grant No.: RG122/14 and RG175/15).

References

[1] P. Li, Z. Wang, N. Petrinic, C.R. Siviour, Deformation behaviour of stainless steel microlattice structures by selective laser melting, Mater. Sci. Eng. A, 614 (2014) 116-121.

[2] X. Tang, V. Prakash, J.J. Lewandowski, G.W. Koolstra, H.N.G. Wadley, Inertial stabilization of buckling at high rates of loading and low test temperatures: Implications for dynamic crush resistance of aluminum-alloy-based sandwich plates with lattice core, Acta Mater., 55 (2007) 2829-2840.

[3] H.N.G. Wadley, N.A. Fleck, A.G. Evans, Fabrication and structural performance of periodic cellular metal sandwich structures, Compos. Sci. Technol., 63 (2003) 2331-2343.

[4] C.L. Qiu, S. Yue, N.J.E. Adkins, M. Ward, H. Hassanin, P.D. Lee, P.J. Withers, M.M. Attallah, Influence of processing conditions on strut structure and compressive properties of cellular lattice structures fabricated by selective laser melting, Mater. Sci. Eng. A, 628 (2015) 188-197.

[5] J. Zhou, P. Shrotriya, W.O. Soboyejo, On the deformation of aluminum lattice block structures: from struts to structures, Mech. Mater., 36 (2004) 723-737.

[6] R.A.W. Mines, On the characterisation of foam and micro-lattice materials used in sandwich construction, Strain, 44 (2008) 71-83.

[7] R. Gumruk, R.A.W. Mines, Compressive behaviour of stainless steel micro-lattice structures, Int. J. Mech. Sci., 68 (2013) 125-139.

[8] P. Li, Constitutive and failure behaviour in selective laser melted stainless steel for microlattice structures, Mater. Sci. Eng. A, 622 (2015) 114-120.

[9] H.D. Carlton, J. Lind, M.C. Messner, N.A. Volkoff-Shoemaker, H.S. Barnard, N.R. Barton, M. Kumar, Mapping local deformation behavior in single cell metal lattice structures, Acta Mater., 129 (2017) 239-250.

[10] M. Leary, M. Mazur, J. Elambasseril, M. McMillan, T. Chirent, Y.Y. Sun, M. Qian, M. Easton, M. Brandt, Selective laser melting (SLM) of AlSi12Mg lattice structures, Mater. Des., 98 (2016) 344-357.

[11] M. Mazur, M. Leary, S.J. Sun, M. Vcelka, D. Shidid, M. Brandt, Deformation and failure behaviour of Ti-6Al-4V lattice structures manufactured by selective laser melting (SLM), Int. J. Adv. Manuf. Technol., 84 (2016) 1391-1411.

[12] B. Vrancken, L. Thijs, J.P. Kruth, J. Van Humbeeck, Microstructure and mechanical properties of a novel beta titanium metallic composite by selective laser melting, Acta Mater., 68 (2014) 150-158.

[13] L.C. Zhang, D. Klemm, J. Eckert, Y.L. Hao, T.B. Sercombe, Manufacture by selective laser melting and mechanical behavior of a biomedical Ti-24Nb-4Zr-8Sn alloy, Scr. Mater., 65 (2011) 21-24.

[14] I. Maskery, N.T. Aboulkhair, A.O. Aremu, C.J. Tuck, I.A. Ashcroft, R.D. Wildman, R.J.M. Hague, A mechanical property evaluation of graded density Al-Si10-Mg lattice structures manufactured by selective laser melting, Mater. Sci. Eng. A, 670 (2016) 264-274.

[15] D.K. Do, P. Li, The effect of laser energy input on the microstructure, physical and mechanical properties of Ti-6Al-4V alloys by selective laser melting, Virtual Phys. Prototyp., 11 (2016) 41-47.

[16] N. Read, W. Wang, K. Essa, M.M. Attallah, Selective laser melting of AlSi10Mg alloy: Process optimisation and mechanical properties development, Mater. Des., 65 (2015) 417-424.

[17] S. Tsopanos, R.A.W. Mines, S. McKown, Y. Shen, W.J. Cantwell, W. Brooks, C.J. Sutcliffe, The Influence of Processing Parameters on the Mechanical Properties of Selectively Laser Melted Stainless Steel Microlattice Structures, J. Manuf. Sci. Eng. – Trans. ASME, 132 (2010).

[18] B. Song, S.J. Dong, H.L. Liao, C. Coddet, Process parameter selection for selective laser melting of Ti6Al4V based on temperature distribution simulation and experimental sintering, Int. J. Adv. Manuf. Technol., 61 (2012) 967-974.

[19] I. Yadroitsev, I. Yadroitsava, P. Bertrand, I. Smurov, Factor analysis of selective laser melting process parameters and geometrical characteristics of synthesized single tracks, Rapid Prototyping J., 18 (2012) 201-208.

[20] L.E. Murr, S.A. Quinones, S.M. Gaytan, M.I. Lopez, A. Rodela, E.Y. Martinez, D.H. Hernandez, E. Martinez, F. Medina, R.B. Wicker, Microstructure and mechanical behavior of Ti-6Al-4V produced by rapid-layer manufacturing, for biomedical applications, J. Mech. Behav. Biomed. Mater., 2 (2009) 20-32.

[21] B. Song, S.J. Dong, B.C. Zhang, H.L. Liao, C. Coddet, Effects of processing parameters on microstructure and mechanical property of selective laser melted Ti6Al4V, Mater. Des., 35 (2012) 120-125.

[22] L. Thijs, F. Verhaeghe, T. Craeghs, J.V. Humbeeck, J.-P. Kruth, A study of the microstructural evolution during selective laser melting of Ti–6Al–4V, Acta Mater., 58 (2010) 3303-3312.

[23] B. Vrancken, L. Thijs, J.P. Kruth, J. Van Humbeeck, Heat treatment of Ti6Al4V produced by Selective Laser Melting: Microstructure and mechanical properties, J. Alloys Compd., 541 (2012) 177-185.

[24] M. Smith, Z. Guan, W.J. Cantwell, Finite element modelling of the compressive response of lattice structures manufactured using the selective laser melting technique, Int. J. Mech. Sci., 67 (2013) 28-41.

[25] A.C. Kaya, P. Zaslansky, A. Nikolaus, C. Fleck, Tensile failure observations in sintered steel foam struts revealed by sub-micron contrast-enhanced microtomography, Mater. Des., 105 (2016) 190-200.

[26] N. Chawla, X. Deng, Microstructure and mechanical behavior of porous sintered steels, Mater. Sci. Eng. A, 390 (2005) 98-112.

[27] R. Huang, P. Li, T. Liu, X-ray microtomography and finite element modelling of compressive failure mechanism in cenosphere epoxy syntactic foams, Compos. Struct., 140 (2016) 157-165.

[28] G.R. Johnson, W.H. Cook, Fracture characteristics of three metals subjected to various strains, strain rates, temperatures and pressures, Eng. Fract. Mech., 21 (1985) 31-48.

[29] T. Borvik, O.S. Hopperstad, S. Dey, E. Pizzinato, M. Langseth, C. Albertini, Strength and ductility of Weldox 460 E steel at high strain rates, elevated temperatures and various stress triaxialities, Eng. Fract. Mech., 72 (2005) 1071-1087.

[30] N.S.K. Ho, P. Li, S. Raghavan, T. Li, The effect of slurry composition on the microstructure and mechanical properties of open-cell Inconel foams manufactured by the slurry coating technique, Mater. Sci. Eng. A, 687 (2017) 123-130.

List of Tables

Aluminium	Vanadium	Iron	Oxygen	Nitrogen	Carbon	Hydrogen	Titanium
6.46	4.24	0.17	0.094	0.01	0.007	0.002	balance

A (MPa)	B (MPa)	n	D_1	D_2	D_3
997	746	0.325	0.005	0.43	-0.48

List of Figures

Fig. 6 (a) The nominal stress–strain curves of a typical SLM Ti-6Al-4V strut with the nominal diameter 600 μm, and (b) the deformation history at three strain stages i–iii as indicated in the curve and at the final fracture. Note that the dashed curve as measured directly in INSTRON is compared to the solid curve with symbols as corrected with accurate strains from the optical images.

Fig. 7 (a–e) The representative and average nominal stress–strain curves of SLM Ti-6Al-4V struts with different nominal diameters; and (f) the final average curve (dashed) calculated from the individual averages for the struts with different diameters.

Fig. 8 SEM images of (a–c) the fracture surfaces of SLM Ti-6Al-4V struts with different diameters and (d) the typical dimples on the fracture surfaces. Note that the right figure in (a–c) is the high magnification SEM image of the fracture initiation site indicated by the arrow in the left figure.

Fig. 9 The J–C hardening model for SLM Ti-6Al-4V alloys, fitted from the measured average stress–strain data. The extrapolated J–C curve is compared with the measured data at fracture.

Fig. 10 The J–C failure model for SLM Ti-6Al-4V alloys, fitted from the experimental data.

Fig. 11 (a) The geometrical model (left) of the SLM Ti-6Al-4V microlattice structure with 6×6×6 BCC unit cells (right), and (b) comparison of the predicted and experimentally measured deformation in the microlattice at the strain of 0.1 during the uniaxial compression.

Fig. 12 Comparison of the predicted and experimentally measured stress–strain curves of SLM Ti-6Al-4V microlattices subjected to uniaxial compression.

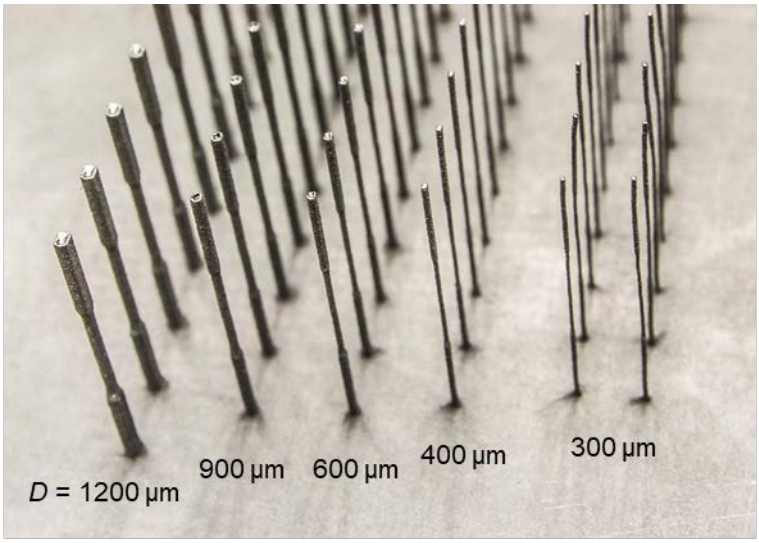

Figure 1: Selective laser melted (SLM) Ti-6Al-4V struts with the different nominal gauge diameters (D = 300, 400, 600, 900 and 1200 µm) for tension tests.

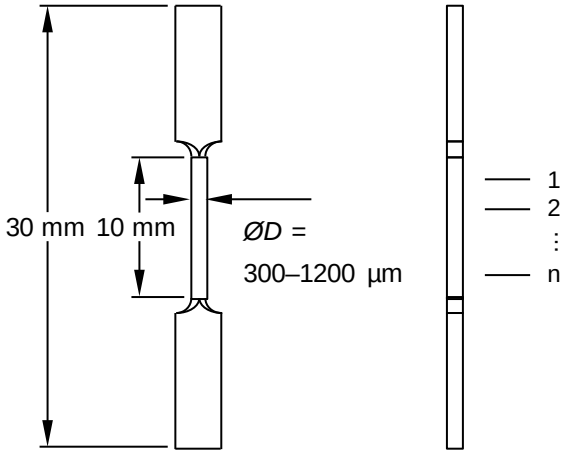

Figure 2: Schematic of the SLM strut with the cylindrical gauge and flat ends for tension tests.

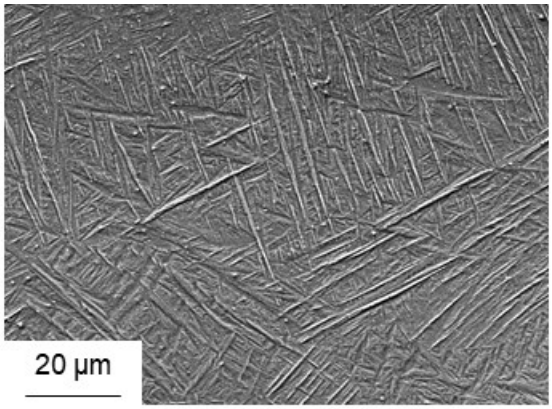

Figure 3: SEM image of the typical microstructure of Ti-6Al-4V alloys as manufactured by SLM.

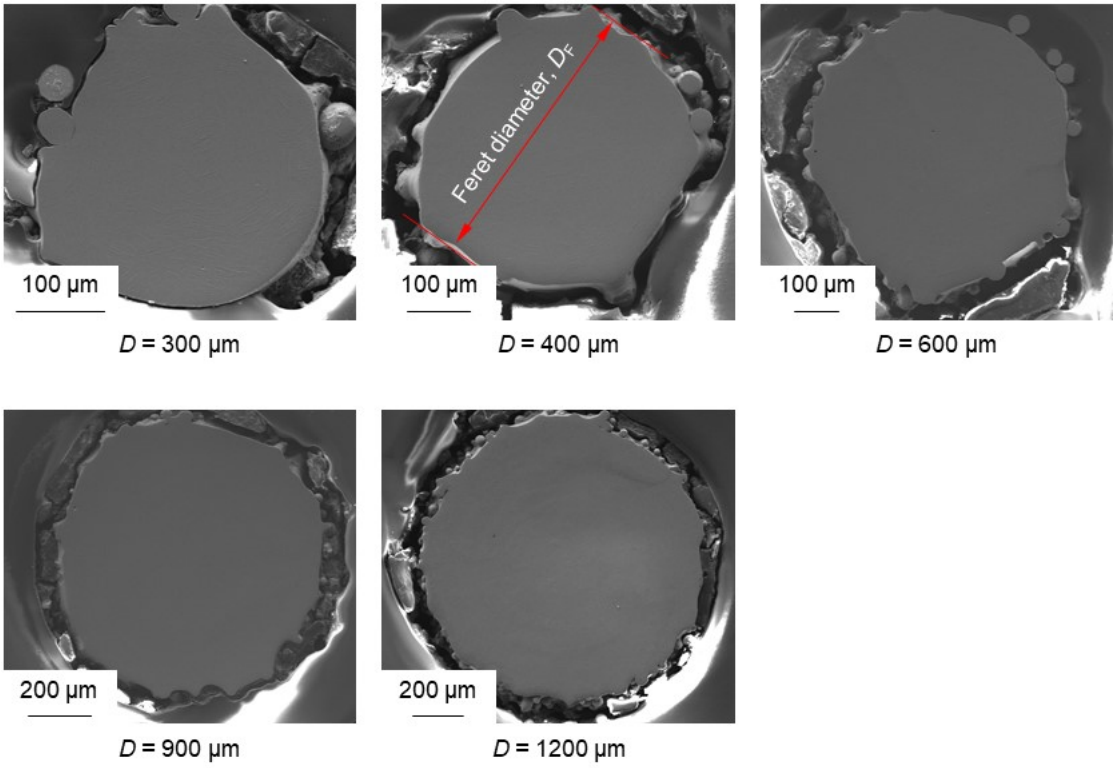

Figure 4: SEM images of the cross sections of individual SLM Ti-6Al-4V struts with different nominal gauge diameters.

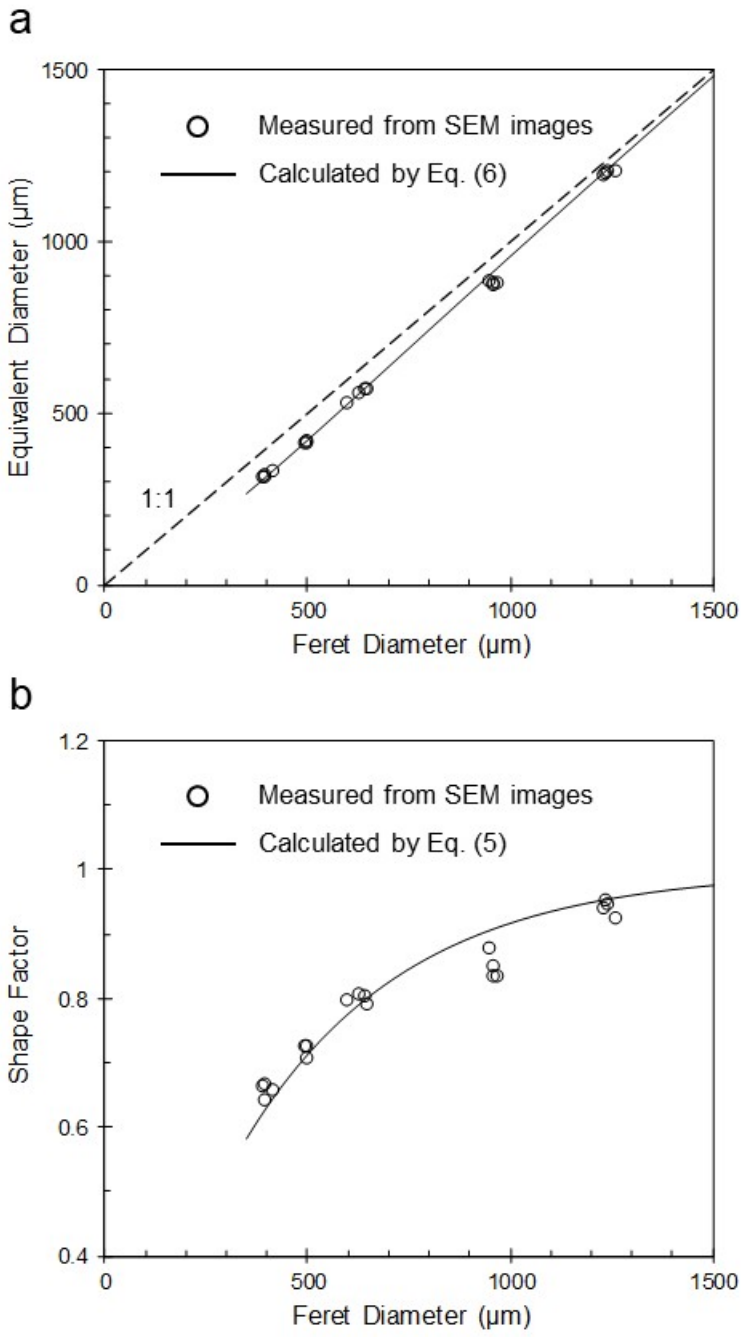

Figure 5: (a) Comparison between the equivalent diameter and the Feret diameter in different cross sections of the SLM Ti-6Al-4V struts; and (b) the shape factor of struts as a function of the Feret diameter.

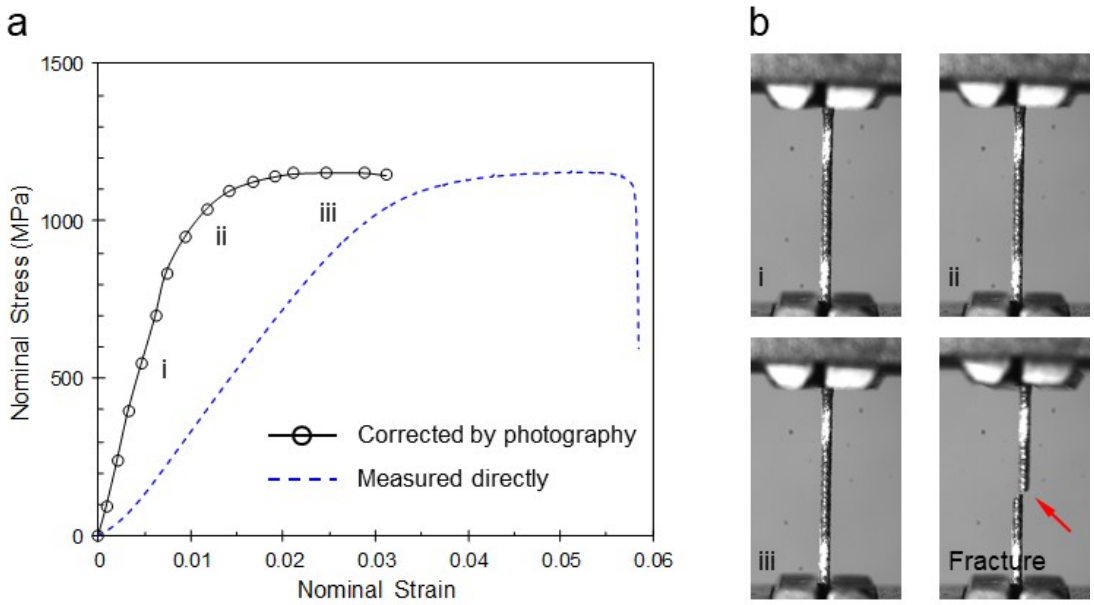

Figure 6: (a) The nominal stress–strain curves of a typical SLM Ti-6Al-4V strut with the nominal diameter 600 μm, and (b) the deformation history at three strain stages i–iii as indicated in the curve and at the final fracture. Note that the dashed curve as measured directly in INSTRON is compared to the solid curve with symbols as corrected with accurate strains from the optical images.

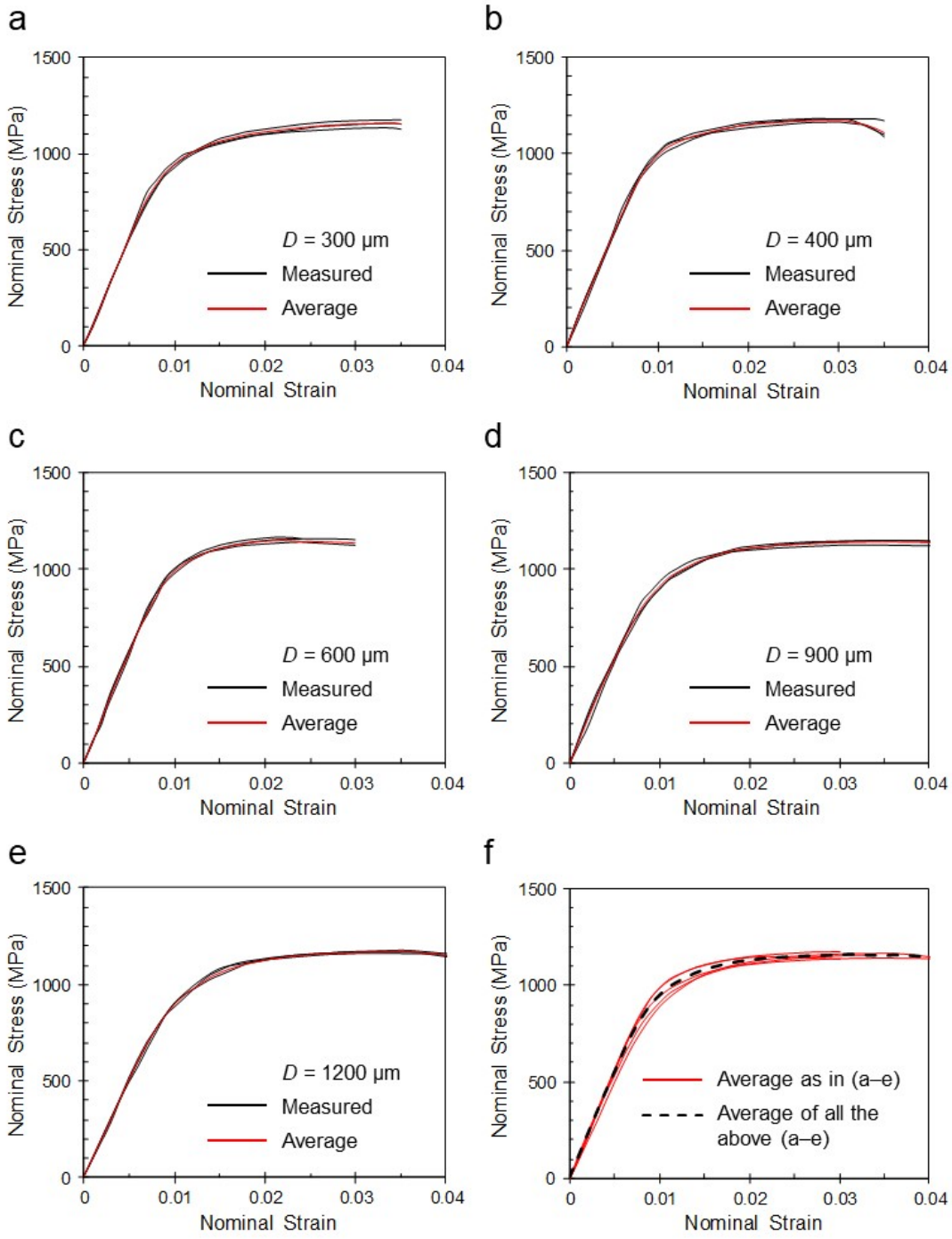

Figure 7: (a–e) The representative and average nominal stress–strain curves of SLM Ti-6Al-4V struts with different nominal diameters; and (f) the final average curve (dashed) calculated from the individual averages for the struts with different diameters.

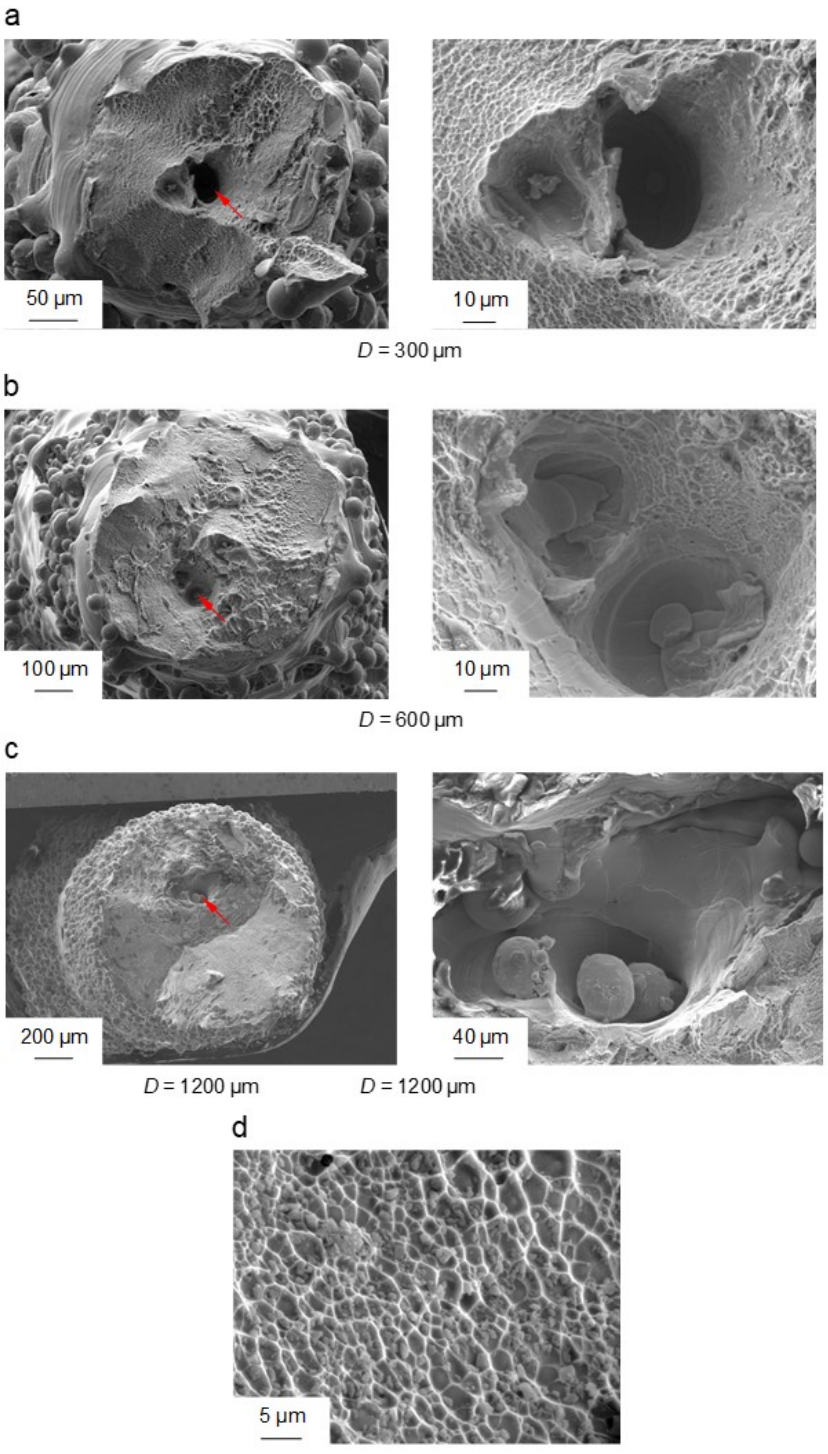

Figure 8: SEM images of (a–c) the fracture surfaces of SLM Ti-6Al-4V struts with different diameters and (d) the typical dimples on the fracture surfaces. Note that the right figure in (a–c) is the high magnification SEM image of the fracture initiation site indicated by the arrow in the left figure.

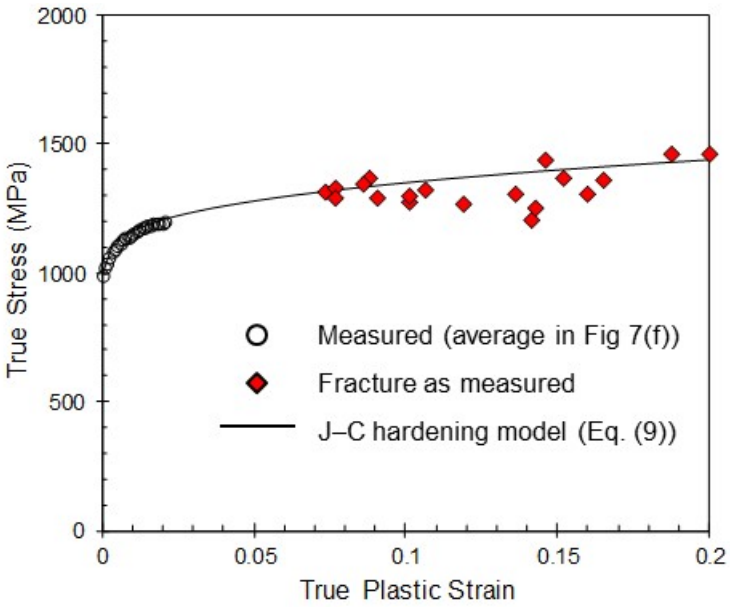

Figure 9: The J–C hardening model for SLM Ti-6Al-4V alloys, fitted from the measured average stress–strain data. The extrapolated J–C curve is compared with the measured data at fracture.

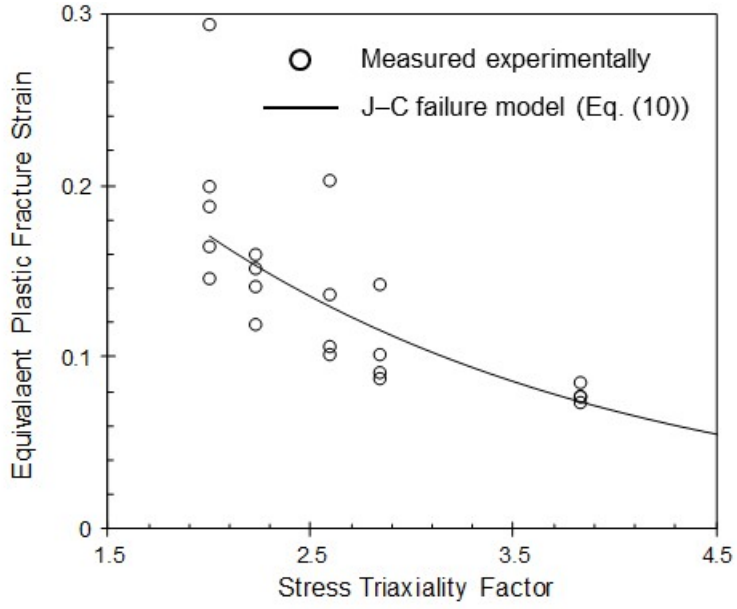

Figure 10: The J–C failure model for SLM Ti-6Al-4V alloys, fitted from the experimental data.

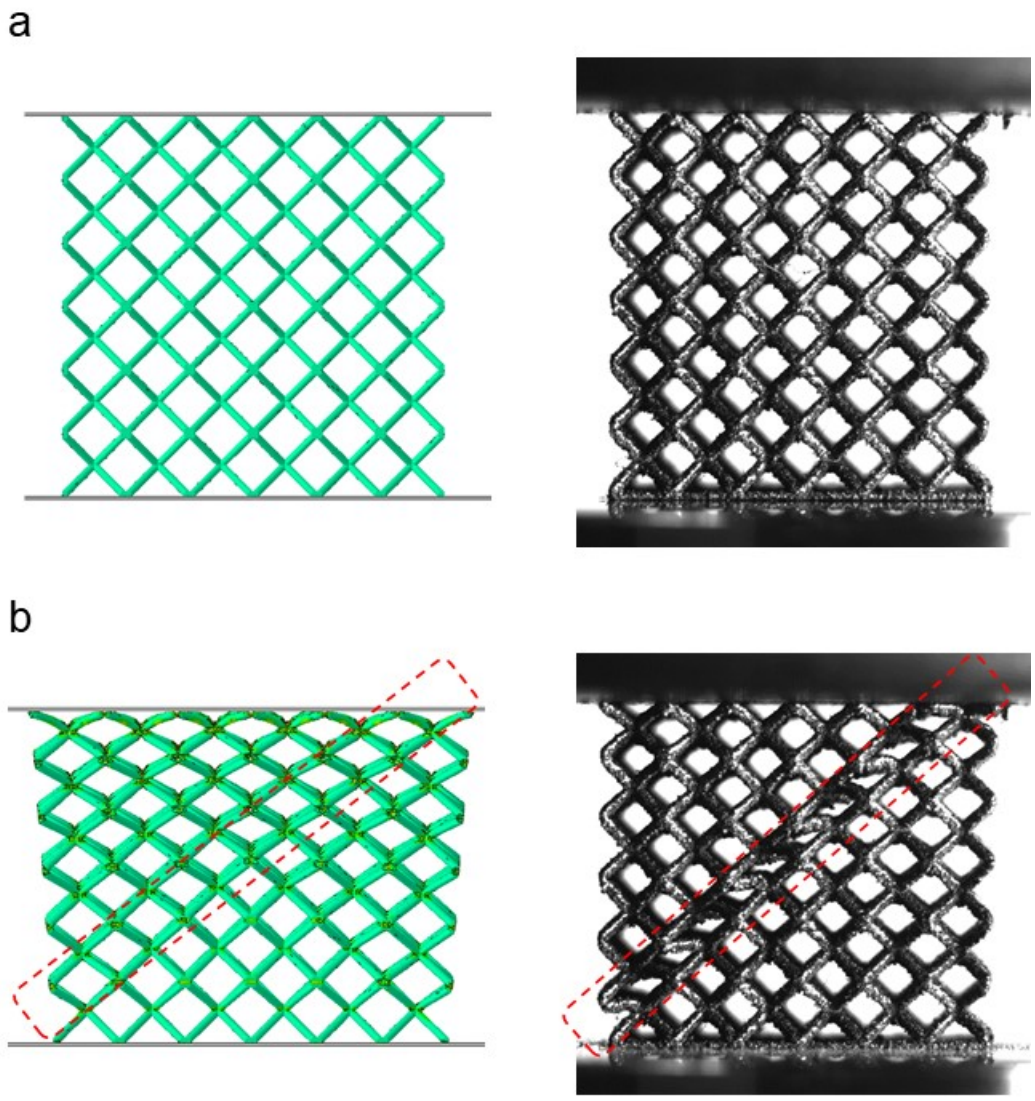

Figure 11: (a) The geometrical model (left) of the SLM Ti-6Al-4V microlattice structure with 6×6×6 BCC unit cells (right), and (b) comparison of the predicted and experimentally measured deformation in the microlattice at the strain of 0.1 during the uniaxial compression.

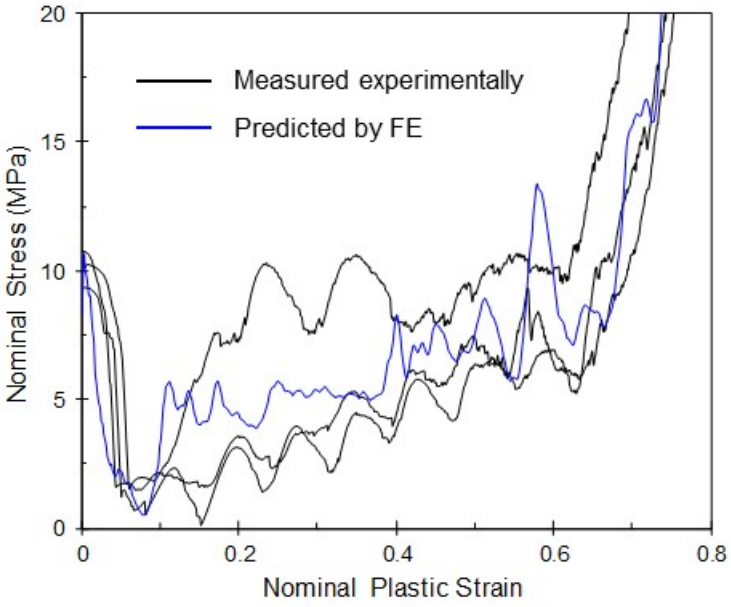

Figure 12: Comparison of the predicted and experimentally measured stress–strain curves of SLM Ti-6Al-4V microlattices subjected to uniaxial compression.